Supporting Information: Optoelectronic synapses realized on large scale continuous $MoSe_2$ with Te doping induced tunable memory function

Yongqi Hu,[#a] Yunan Lin,[#a] Xutao Zhang,[a] Yanlu Zhao,[a] Lan Li,[a] Yinuo Zhang,[a] Hong Lei [b],Yi Pan[* a]

[a] Center for Spintronics and Quantum Systems, State Key Laboratory for Mechanical Behavior of Materials, Xi'an Jiaotong University, Xi'an 710049, China.

[b] Shaanxi Institute for Pediatric Diseases, Xi'an Children's Hospital, Affiliated Children's Hospital of Xi'an Jiaotong University, Xi'an, Shaanxi 710003, China

[#] Both authors contributed equally to this work

[*] Email: yi.pan@xjtu.edu.cn

Fig. S1 shows the process diagram of chemical vapor deposition (CVD) growth. Initially, the surface hydrophilicity of the substrate is enhanced by plasma treatment, which provides a prerequisite for the uniform distribution of the precursor. Subsequently, the Na_2MoO_4 precursor is uniformly distributed on the substrate surface by spin - coating. Finally, the growth of the material is carried out in a tube furnace.

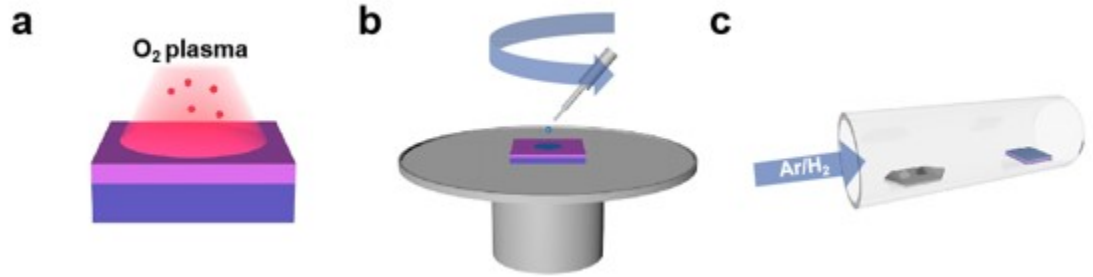

Fig. S1. Schematic diagram of the growth steps. (a) oxygen plasma etching of SiO_2/Si substrate; (b) spin coating of precursor solution; (c) tolerization at high temperature in a hot wall tube furnace.

Fig. S2 shows the distinct morphologies presented by the growth of materials with different precursor distributions. When the precursor is enriched, the growth is more inclined towards vertical growth rather than horizontal growth.

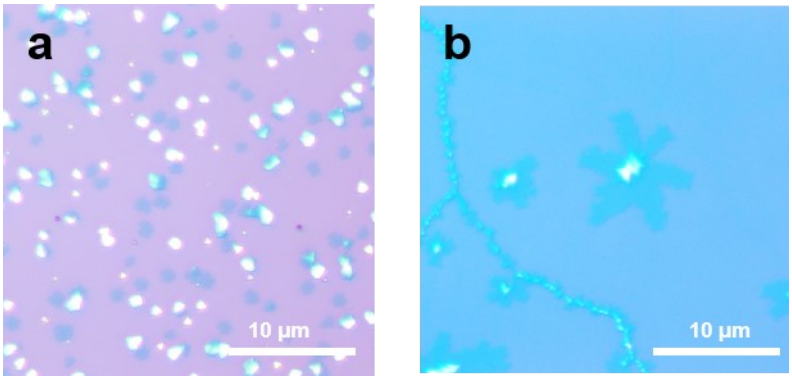

Fig. S2. Optical micrographs of materials resulting from different precursor distributions: high concentration on the left (a) and appropriate concentration on the right (b).

Fig. S3a shows the AFM results of the SiO_2/Si substrate after spin-coating with the Na_2MoO_4 precursor. Multiple regions on the substrate were analyzed, revealing a uniform RMS roughness of 5.45 nm across the entire wafer. This uniformity confirms the homogeneous distribution of the spin-coated precursor, which serves as a critical foundation for wafer-scale Te-doped $MoSe_2$ growth. As shown in Fig. S3b, for the grown Te-doped $MoSe_2$ film, AFM characterization indicated overall uniformity, but the presence of small nucleation centers introduced isolated protrusions on the surface. The RMS roughness increased to 1.81 nm due to these protrusions. However, when focusing on regions with minimal nucleation centers, the RMS roughness dropped to 0.283 nm. This result demonstrates the high-quality uniformity of the Te-doped $MoSe_2$ film itself, with the observed surface irregularities attributed to localized nucleation rather than systematic defects.

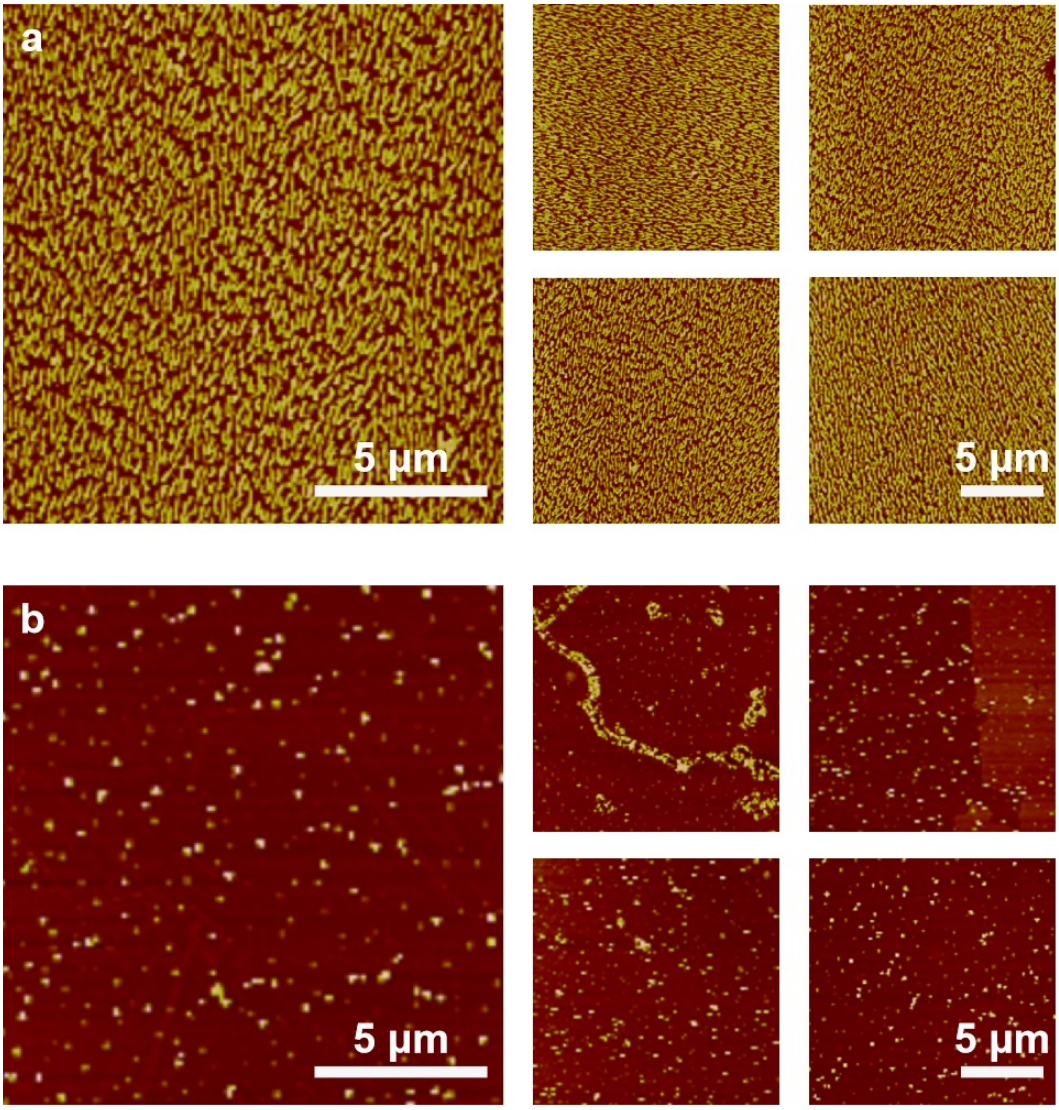

Fig. S3. AFM image of the (a) Na_2MoO_4 precursor and (b) the surface of Te - doped $MoSe_2$.

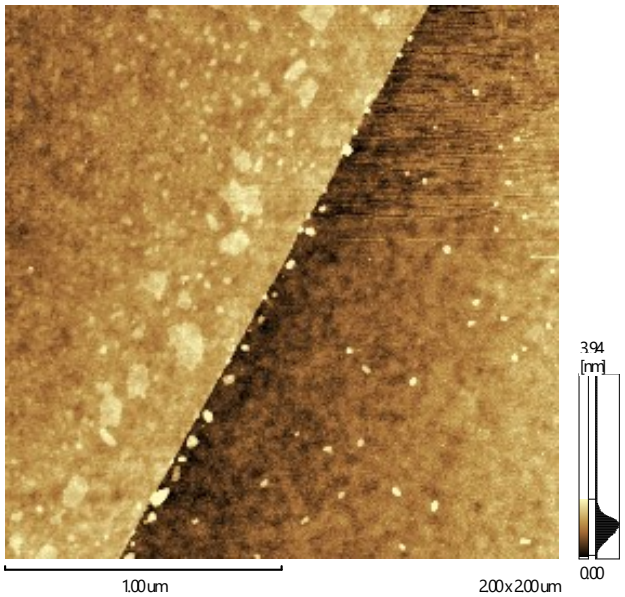

Fig. S4. Large area image of AFM.

In Fig. S5, in accordance with the secondary growth at grain boundaries, different domains of the materials were filled with distinct colors.

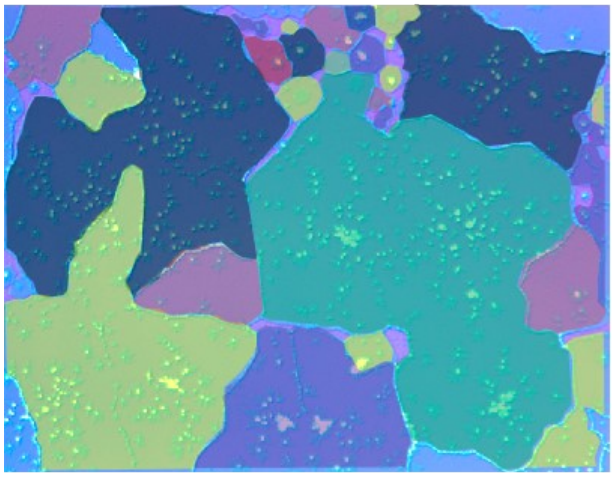

Fig. S5. A photograph showcasing the uniformity and size of the Te-doped $MoSe_2$ film grown over a 2-inch wafer using the optimized CVD method.

Fig. S6 shows continuous films grown in different batches. The domain sizes of the materials were statistically analyzed through the segmentation of grain boundaries. Among them, the side length of the largest domain can reach 500 micrometers, with an average value of 198.12 micrometers.

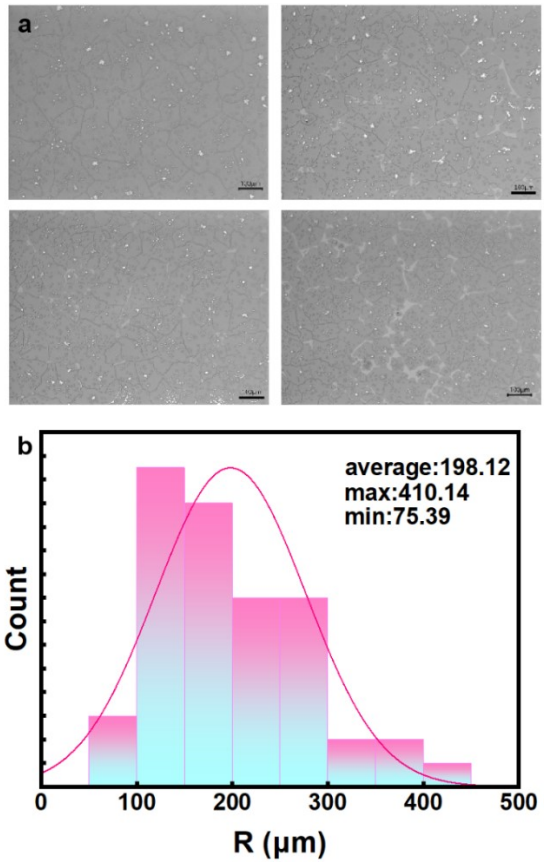

Fig. S6. Statistics of single-domain dimensions of different samples. (a) Optical microscopy images of different continuous film samples. (b) Statistical results of domain segmentation based on the grain boundaries of continuous films.

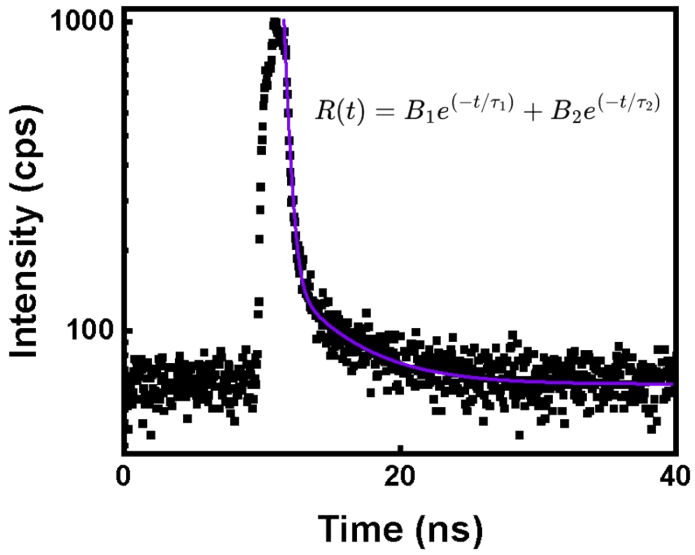

Fig. S7. Time resolved PL signals of Te-doped $MoSe_2$.

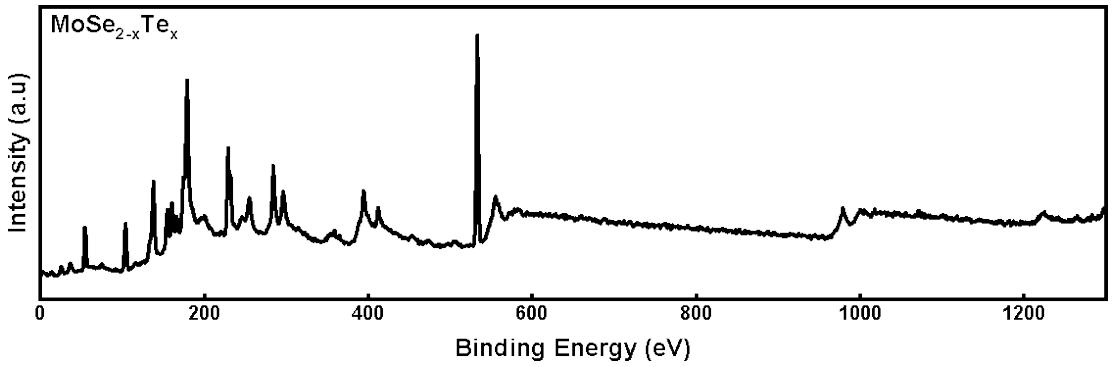

Fig. S8. XPS survey scan is captured on the as-synthesized Te-doped $MoSe_2$ flakes deposited on the Si/SiO_2 substrate.

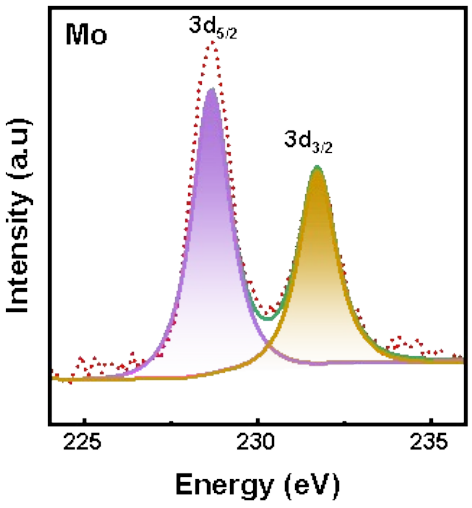

Fig. S9. XPS spectra of Mo peak.

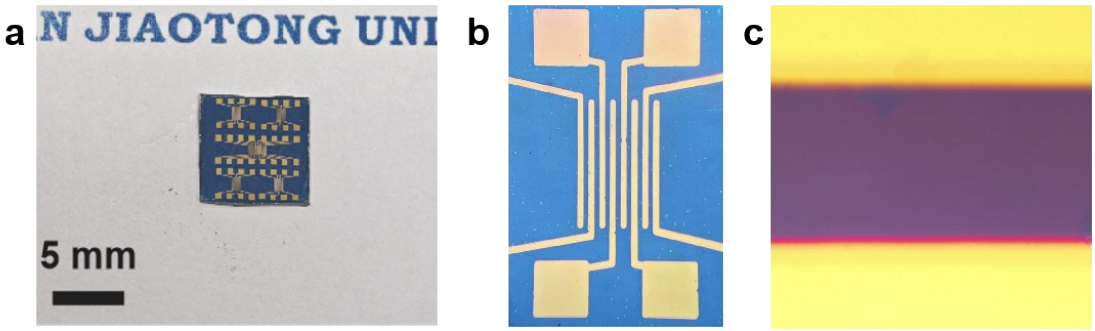

Fig. S10. Photographs and microscopy images of the fabricated Te-doped $MoSe_2$ array device. (a) Optical photograph of the device on a 5 mm scale. (b) Close-up of the patterned electrodes deposited on the Te-doped $MoSe_2$ film. (c) Optical microscopy image showing the uniformity of the continuous Te-doped $MoSe_2$ film.

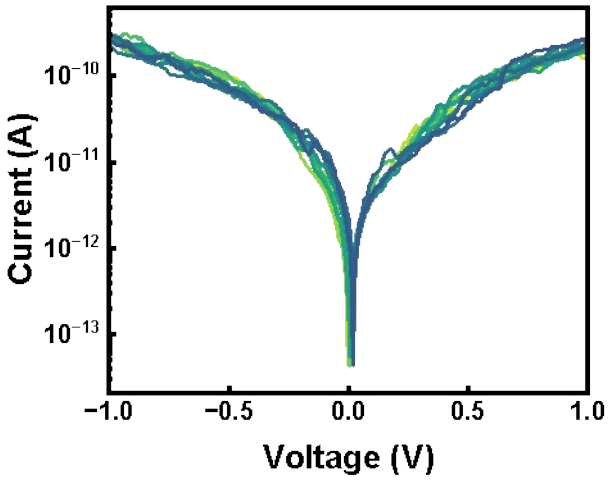

Fig. S11. Representative I-V curves obtained from different groups of $MoSe_2$ synaptic device.

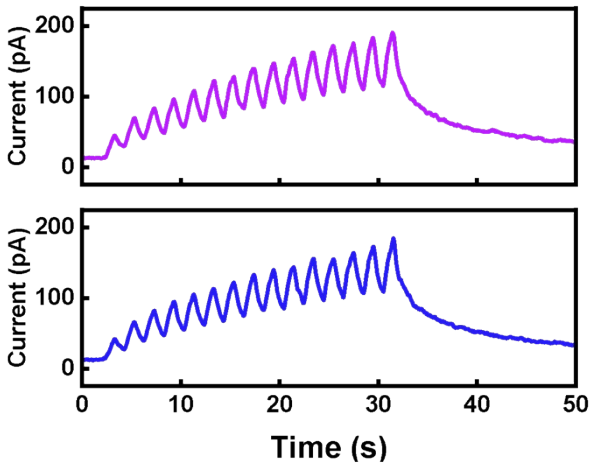

Fig. S12. I–t curves of the $MoSe_2$ synaptic device. Upper panel: fresh device; Lower Panel: after 3 months.

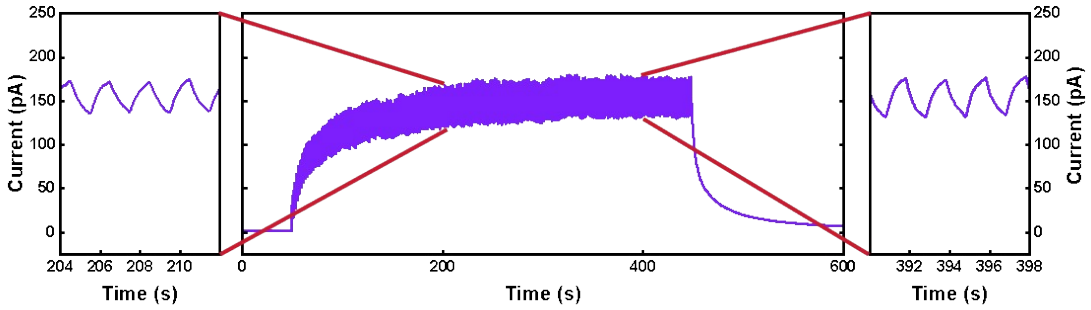

Fig. S13. Cycle-to-cycle variations of $MoSe_2$ synaptic device with repeated on/off for 200 s.

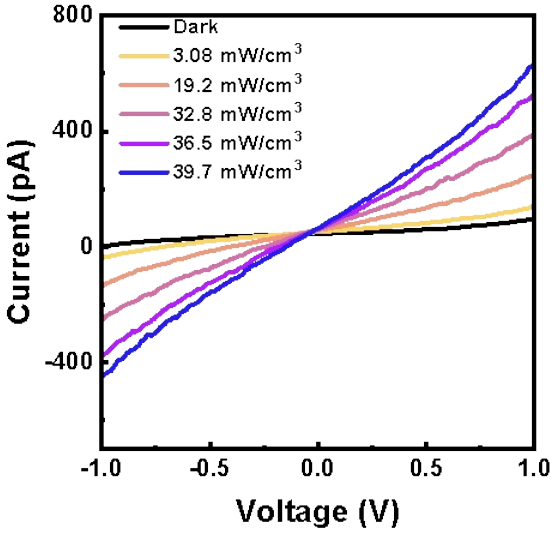

Fig. S14. Current-voltage (I-V) characteristics of the device under different ultraviolet (UV) light intensities.

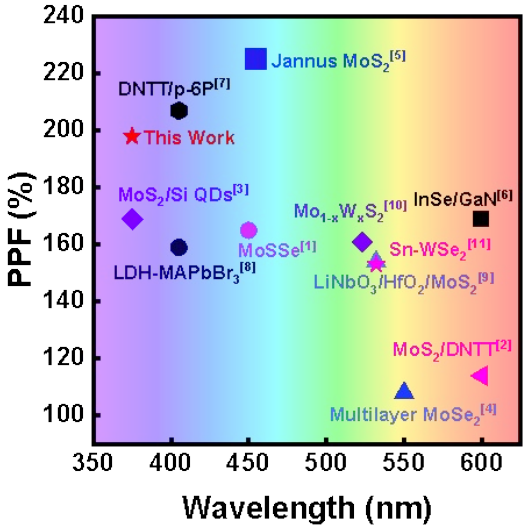

Fig. S15. Comparison of the PPF of TMDs-based optical synaptic device.[1-11]

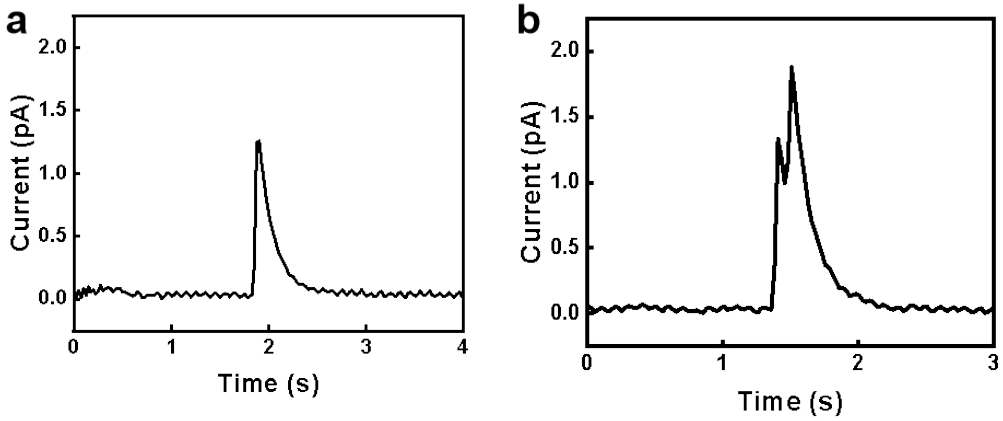

Fig. S16. (a) Single-pulse energy consumption and (b) pulse feasibility tests under 0.001V bias condition using a 405nm laser with 36.38 μW/cm^2 intensity.

Device	Wavelength (nm)	Energy consumption	PPF(%)	Ref.
Te-doped $MoSe_2$	365	3 pJ/0.06 fJ	197	this work
MoSSe	450	>100 pJ	166	[1]
MoS_2/DNTT	600	0.4 fJ	114	[2]
Si QDs/MoS_2	375	>100 pJ	169	[3]
$MoSe_2$ Moiré Superlattice	550	7.2 pJ	107.8	[4]
Janus MoS_2	455	>100 pJ	225	[5]
InSe/GaN	600	>100 pJ	169	[6]
DNTT/p-6P	450	0.54 fJ	207	[7]
LDH-$MAPbBr_3$	405	50 pJ	159	[8]
$LiNbO_3$/HfO_2/MoS_2	532	>100 pJ	154	[9]
$Mo_{1-x}W_xS_2$	523	>100 pJ	161	[10]
Sn-WSe_2	532	0.1 fJ	153	[11]

Table S1. Comparison of the energy consumption and PPF of this work and those of the previously published organic artificial photonic synapses.

Reference

1 J. Meng, T. Wang, H. Zhu, L. Ji, W. Bao, P. Zhou, L. Chen, Q. Q. Sun and D. W. Zhang, *Nano Lett*, 2022, **22**, 81-89.

2 J. Wang, B. Yang, S. Dai, P. Guo, Y. Gao, L. Li, Z. Guo, J. Zhang, J. Zhang and J. Huang, *Advanced Materials Technologies*, 2023, **8**, 2300449.

3 Y. Wang, K. Wang, X. Hu, Y. Wang, W. Gao, Y. Zhang, Z. Liu, Y. Zheng, K. Xu, D. Yang and X. Pi, *ACS Nano*, 2023, **17**, 3696-3704.

4 H. Yang, Y. Hu, X. Zhang, Y. Ding, S. Wang, Z. Su, Y. Shuai and P. Hu, *Advanced Functional Materials*, 2023, **34**, 2308149.

5 Y. Wang, B. Han, M. Mayor and P. Samorì, *Advanced Materials*, 2024, **36**, 2307359.

6 X. Miao, Y. Zhang, Y. Lin, H. Lei, T. Min and Y. Pan, *Advanced Optical Materials*, 2024, **12**, 2400358.

7 E. Ercan, C.-C. Hung, G.-S. Li, Y.-F. Yang, Y.-C. Lin and W.-C. Chen, *Nanoscale Horizons*, 2023, **8**, 632-640.

8 Q. Chen, J. Cao, Z. Yang, Z. Wang, J. Wang, S. Yu, C. Hao, N. Wang, H. Li and X. Huang, *Nanoscale Horizons*, 2024, **9**, 1023-1029.

9 Y. Wang, T. Zhou, Y. Cui, M. Xu, M. Zhang, K. Tang, X. Chen, H. Tian, C. Yin, J. Huang, C. Yan and X. Wang, *Advanced Functional Materials*, 2024, **34**, 2400039.

10 B. Pan, L. Zhang, S. Lan, Y. Hong, J. Liang, L. Deng, T. Taniguchi, K. Watanabe, X. Gao, J. L. Xu, Y. N. Zhong, J. Miao, Y. Ye, L. J. Li, S. Wang, W. Hu, S. D. Wang and P. Wang, *Advanced Functional Materials*, 2025, DOI: 10.1002/adfm.202421337, 2421337.

11 M. Ma, C. Huang, M. Yang, D. He, Y. Pei, Y. Kang, W. Li, C. Lei and X. Xiao, *Small*, 2024, **20**, 2406402.